Magnetic anisotropy in the frustrated spin-chain compound β-TeVO$_4$

F. Weickert,[1,*] N. Harrison,[1] B. L. Scott,[2] M. Jaime,[1] A. Leitmäe,[3] I. Heinmaa,[3] R. Stern,[3] O. Janson,[3,4,5] H. Berger,[6]
H. Rosner,[4] and A. A. Tsirlin[3,4,7,†]

[1]*MPA-CMMS, Los Alamos National Laboratory, Los Alamos, New Mexico 87545, USA*
[2]*MPA-11, Los Alamos National Laboratory, Los Alamos, New Mexico 87545, USA*
[3]*National Institute of Chemical Physics and Biophysics, 12618 Tallinn, Estonia*
[4]*Max Planck Institute for Chemical Physics of Solids, 01187 Dresden, Germany*
[5]*Institute of Solid State Physics, TU Wien, 1040 Vienna, Austria*
[6]*Ecole Polytechnique Fédérale de Lausanne, Lausanne CH-1015, Switzerland*
[7]*Experimental Physics VI, Center for Electronic Correlations and Magnetism, Institute of Physics,*
University of Augsburg, 86135 Augsburg, Germany

Isotropic and anisotropic magnetic behavior of the frustrated spin-chain compound β-TeVO$_4$ is reported. Three magnetic transitions observed in zero magnetic field are tracked in fields applied along different crystallographic directions using magnetization, heat capacity, and magnetostriction measurements. Qualitatively different temperature-field diagrams are obtained below 10 T for the field applied along a or b and along c, respectively. In contrast, a nearly isotropic high-field phase emerges above 18 T and persists up to the saturation that occurs around 22.5 T. Upon cooling in low fields, the transitions at T_{N1} and T_{N2} toward the spin-density-wave and stripe phases are of the second order, whereas the transition at T_{N3} toward the helical state is of the first order and entails a lattice component. Our microscopic analysis identifies frustrated J_1-J_2 spin chains with a sizable antiferromagnetic interchain coupling in the bc plane and ferromagnetic couplings along the a direction. The competition between these ferromagnetic interchain couplings and the helical order within the chain underlies the incommensurate order along the a direction, as observed experimentally. While a helical state is triggered by the competition between J_1 and J_2 within the chain, the plane of the helix is not uniquely defined because of competing magnetic anisotropies. Using high-resolution synchrotron diffraction and ^{125}Te nuclear magnetic resonance, we also demonstrate that the crystal structure of β-TeVO$_4$ does not change down to 10 K, and the orbital state of V^{4+} is preserved.

I. INTRODUCTION

Frustrated (zigzag) spin-$\frac{1}{2}$ chains with competing nearest-neighbor ferromagnetic (J_1) and next-nearest-neighbor antiferromagnetic (J_2) couplings reveal rich physics at low temperatures and in applied magnetic fields. When the chains are coupled in three dimensions, helical order arises in zero field for $J_2/|J_1| > \frac{1}{4}$ [1,2]. While the helical order itself gives rise to a very unusual phenomenon of magnetic-field-induced ferroelectricity [3–5], further interesting effects occur when stronger magnetic fields break this order down. LiCuVO$_4$, one of the best studied frustrated-chain materials [6], undergoes a first-order transition around 8.5 T from the helically-ordered phase toward a spin-density-wave (SDW) phase, where magnetic moments align with the field, and the length of the moment is modulated [7,8]. The detailed nature of this phase is, however, debated [9], along with the putative nematic phase appearing around 40 T right before saturation [10,11]. Additionally, different types of multipolar order are expected for the J_1-J_2 chains in the applied magnetic field [12–14].

β-TeVO$_4$ is a candidate frustrated-chain material with spin-$\frac{1}{2}$ (Fig. 1). Its magnetic behavior was initially described within the model of a uniform spin-$\frac{1}{2}$ chain [15], although the presence of three low-temperature transitions at $T_{N1} \simeq 4.7$ K,

$T_{N2} \simeq 3.3$ K, and $T_{N3} \simeq 2.3$ K in an applied magnetic field as weak as 0.02 T clearly indicates a more complex interaction topology. Recently, Saúl and Radtke [16] performed a microscopic analysis of isotropic exchange couplings and concluded that β-TeVO$_4$ is a good realization of the J_1-J_2 chain model with ferromagnetic (FM) J_1 and antiferromagnetic (AFM) J_2. Subsequently, magnetic susceptibility of β-TeVO$_4$ was reanalyzed in the framework of the J_1-J_2 model [17]. Gnezdilov *et al.* [18] reported nonmonotonic evolution of phonon frequencies and speculated on possible structural changes around 150 K and even on a change in the orbital state of V^{4+} at low temperatures. Finally, Pregelj *et al.* [19] performed detailed neutron-scattering experiments in zero field and observed a helical magnetic structure with the propagation vector $\mathbf{k} = (-0.208,0,0.423)$ below T_{N3}. Between T_{N3} and T_{N2}, β-TeVO$_4$ reveals an enigmatic stripelike spin texture, whereas between T_{N2} and T_{N1} a spin-density-wave (SDW) phase akin to the field-induced SDW phase in LiCuVO$_4$ [7,8] has been proposed.

The crystal structure of β-TeVO$_4$ [20] features chains of VO$_5$ polyhedra (Fig. 1). These chains are directed along the crystallographic c axis and linked via asymmetric TeO$_4$ units. The overall structure is centrosymmetric (space group $P2_1/c$), but inversion centers are located between the chains, so that Dzyaloshinsky-Moriya (DM) anisotropy terms are allowed for both J_1 and J_2, which is different from any of the frustrated-chain compounds previously reported. Magnetic anisotropy can have a strong effect on field-induced phase
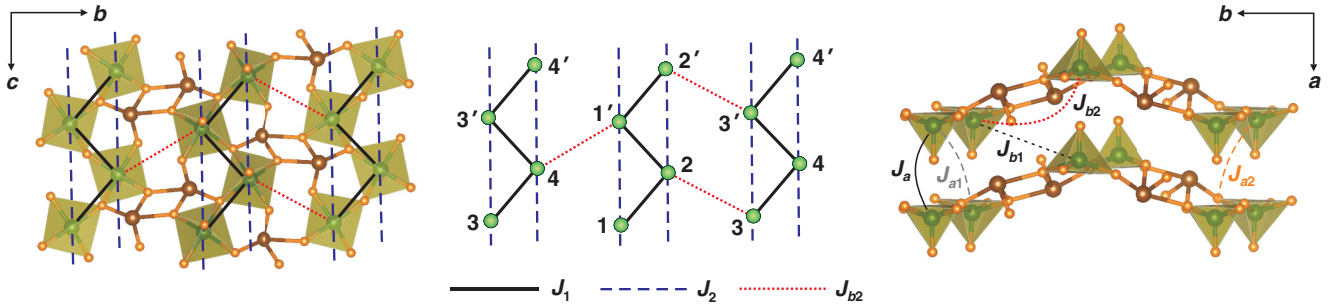
*weickert.ph@gmail.com
†altsirlin@gmail.com

FIG. 1. Crystal structure and magnetic model of β-TeVO$_4$. Left and middle panels: structural and magnetic layers composed of the J_1-J_2 frustrated spin chains. Right panel: interlayer couplings.

transitions and on new phases induced by the magnetic field. For example, linarite PbCu(OH)$_2$SO$_4$, whose symmetry is lower than in LiCuVO$_4$ [21], shows very complex and still poorly understood temperature-field phase diagrams [22] that are weakly reminiscent of those for LiCuVO$_4$.

In the following, we report a combined experimental and microscopic study of β-TeVO$_4$ and address several pending questions concerning this interesting material. In Sec. III A, we report temperature-field phase diagrams for different directions of the applied magnetic field and thus probe magnetic anisotropy in β-TeVO$_4$ experimentally. We show that β-TeVO$_4$ reveals very unusual phase diagrams with the first-order transition toward the helically ordered phase and second-order transitions between other phases. In Secs. III B and III C, we discuss possible structural changes happening in the paramagnetic state and conclude that the overall symmetry of the structure as well as the orbital state of V^{4+} are essentially unchanged down to at least T_{N1}. Finally, in Sec. III D we derive the microscopic spin Hamiltonian of β-TeVO$_4$ and briefly discuss its implications. Our results are summarized in Sec. IV.

II. METHODS

A slab-shaped single crystal [15] of approximate dimensions $5 \times 3 \times 1$ mm^3 was oriented using x-ray scattering and found to have the longest dimension along the crystallographic c axis and the shortest along the a axis, while the intermediate dimension is parallel to the b axis. It was experimentally found that while the cb plane cleaves easily, exposing the chainlike underlying structure, neither the ac nor the ab plane do so.

Thermal expansion at constant magnetic fields and magnetostriction in pulsed magnetic field measurements were accomplished using an optical fiber Bragg grating (FBG) technique described before [23,24]. Here, light reflected at the Bragg wavelength λ_B by a grating inscribed in a telecom 125 μm diameter optical fiber is recorded with a spectrometer furbished with a fast InGaAs line-array camera working at 46 kHz [24] and used to follow the sample dilation as the temperature and/or external magnetic field are changed. For these experiments the fiber was attached to the sample ab plane when studying the strain along the a and b crystallographic directions, and to the ac plane when studying the strain along the c direction.

The magnetization in pulsed magnetic fields to 60 T at constant temperatures was obtained with a sample-extraction magnetometer working to ^{3}He temperatures and calibrated

with measurements in a Quantum Design PPMS system to 14 T. Specific heat measurements at constant magnetic fields were completed in the same PPMS system.

High-resolution x-ray diffraction (XRD) data were collected on the ID31 beamline of the European Synchrotron Radiation Facility (ESRF, Grenoble) using the wavelength of 0.4 Å. A small crystal of β-TeVO$_4$ was crushed, ground into fine powder, and placed into a thin-wall borosilicate glass capillary that was spun during the measurement. The signal was collected by eight Si(111) analyzer crystals. Structure refinements were performed in the JANA2006 program [25], and the resulting crystal structure was visualized using VESTA [26].

All ^{125}Te NMR spectra were recorded on a Bruker AVANCE-II NMR spectrometer at 14.1 T magnetic field using a home-built probe with a single-axis goniometer and He-flow cryostat from JANIS Research Inc. The temperature was monitored and regulated by a LakeShore-332 temperature controller. Each data point was obtained by recording the signal with a spin-echo sequence. The magnetic shift scale was referenced to the ^{125}Te resonance frequency of Me$_2$Te 189.349 MHz.

The microscopic analysis of β-TeVO$_4$ is based on density-functional-theory (DFT) band-structure calculations performed in the FPLO code [27]. Experimental crystal structure obtained from low-temperature XRD has been used, and either the local-density approximation (LDA) [28] or generalized-gradient-approximation (GGA) [29] exchange-correlation potentials were chosen. Isotropic exchange couplings were obtained from two complementary procedures, the LDA-based model analysis and the DFT+U supercell calculations, as further explained in Sec. III D. For the DFT+U calculations, we used supercells doubled along either a or c directions.

Magnetic susceptibility for the J_1-J_2 chain was obtained by combining transfer-matrix renormalization group (TMRG) [30] and exact-diagonalization (ED) simulations for the low- and high-temperature parts of the data, respectively. Exact diagonalization was performed for a finite lattice with $L = 16$ sites and periodic boundary conditions. The use of TMRG helps to eliminate finite-size effects that manifest themselves at low temperatures. Field-dependent magnetization for the J_1-J_2 chain was calculated at zero temperature using the density-matrix renormalization group (DMRG) method. The ED and DMRG simulations were performed in the ALPS simulations package [31].
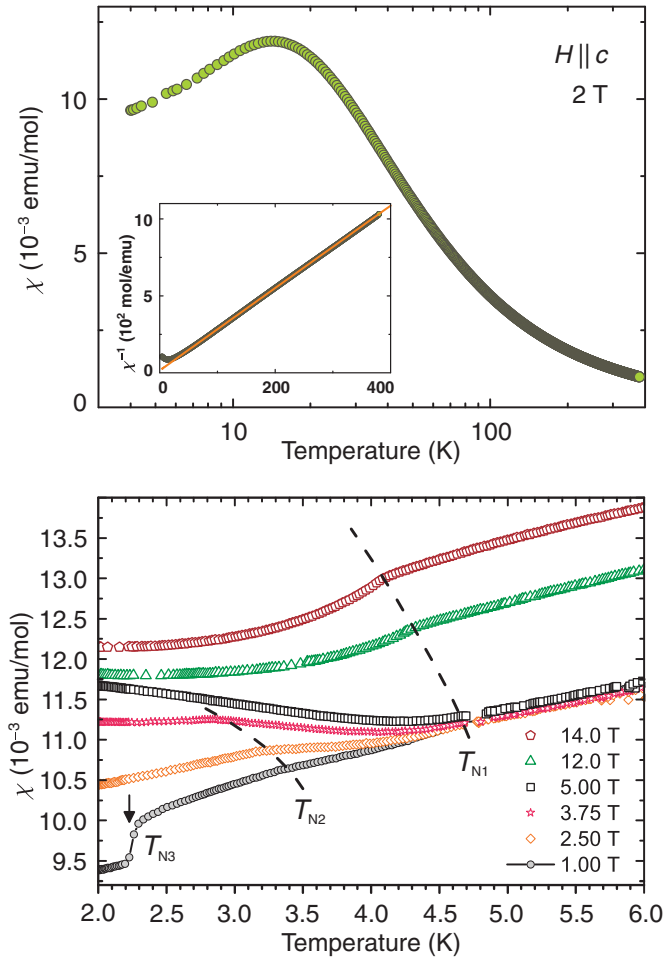
FIG. 2. Top panel: Magnetic susceptibility vs temperature for $H = 2$ T in a wide temperature range. Inset: inverse magnetic susceptibility vs temperature showing Curie-Weiss behavior and fit. Bottom panel: magnetic susceptibility vs temperature in the low-temperature region at constant magnetic fields. Anomalies in $\chi(T)$ are indicated as T_{N1}, T_{N2}, and T_{N3}, and dashed lines are guides to the eye.

III. RESULTS

A. Anisotropic magnetic properties and (T, H) phase diagrams

The magnetic susceptibility (χ) of a single-crystal sample was measured as a function of the temperature at constant magnetic fields between 1 T and 14 T. The results are displayed in Fig. 2. At high temperatures, the magnetic susceptibility follows a Curie-Weiss dependence, while at lower temperatures a clear maximum centered at $T = 14.5$ K [Fig. 2(a)], followed by several smaller anomalies as the temperature is reduced. A Curie-Weiss fit of the data, $\chi = C/(T - \theta)$, in the 100–380 K range [Fig. 2(a), inset] gives a Curie constant $C = 0.374$ emu K mol^{-1} and $\theta_{CW} = -2.1$ K indicating a nearly perfect balance of FM and AFM couplings, in agreement with earlier work [18]. The low-temperature anomalies are more clearly visible when the low temperature range is expanded [Fig. 2(a)]. Three phase transitions were identified as T_{N1}, T_{N2}, and T_{N3} and followed as the magnetic field was increased. While T_{N1} and T_{N2} share characteristics of second-order-like transitions, T_{N3} instead involves a rapid drop in χ suggesting a different,
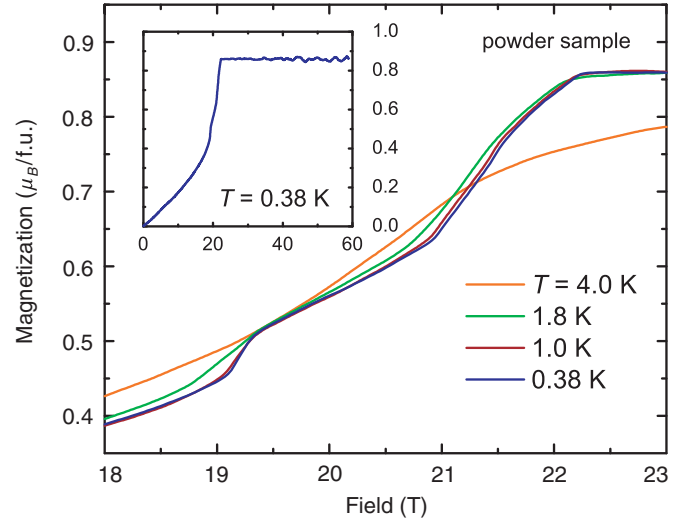

FIG. 3. Magnetization vs magnetic field measured at temperatures between 0.38 K and 4 K in a powder sample. Note saturation at 0.86 μ_B/f.u. Inset: Magnetization vs magnetic field showing the full field range to 60 T.

possibly first-order-like, process. Dashed lines indicate their evolution with applied field.

The magnetization vs field $M(H)$ measured in a powder sample, displayed in Fig. 3, shows $M(H)$ increasing gradually with field. Two small anomalies at 2.5 T and 5.8 T, not visible to the naked eye, are seen at $T = 0.38$ K and two large steps at 19 and 21 T. These anomalies, likely associated with the suppression of low-temperature magnetic order, wash out and eventually vanish as the temperature is increased to 4 K. A saturation magnetization of 0.86 μ_B/f.u. persists to the maximum field of 60 T. Note that the saturation magnetization is somewhat below the value of 1.0 μ_B expected for a spin-$\frac{1}{2}$ system. This might be due to ambiguities in scaling the pulsed-field data against the data collected in static fields.

The specific heat of a 6.2 mg slab-shaped sample was measured in magnetic fields applied along the crystallographic a and b axes. Representative data is displayed in Fig. 4 for different field directions. Particularly interesting are the $H \| b$-axis data: Here, the transition $T_{N3} = 2.3$ K in zero field looks different from the other λ-like transitions, much as in the case of $M(T)$ data, reinforcing the support for a different type of transition. Also, along this direction the transition T_{N1} is observed to split for magnetic fields $H \geqslant 9$ T.

The nature of low-temperature phase transitions in β-TeVO$_4$ can be tested with probes that are sensitive to the crystal lattice, such as thermal expansion and magnetostrain $\Delta L/L(H)$, to gather information on the relevance and strength of spin-lattice correlations. Figure 5 shows a negative thermal expansion along the c direction (μStrain $\equiv 10^{-6}\Delta L/L$), i.e., the sample expands as the temperature drops. Similar behavior was observed for the b direction. Figure 6(a) displays the thermal expansion at constant magnetic field $H = 1$ T, in the low temperature range where the transitions at T_{N1}, T_{N2}, and T_{N3} are clearly visible. While T_{N1} and T_{N2} look like conventional λ-like second-order transitions, T_{N3}, again, looks different. The sharp drop in lattice parameter on cooling resembles a first-order-like transition. It is often the case
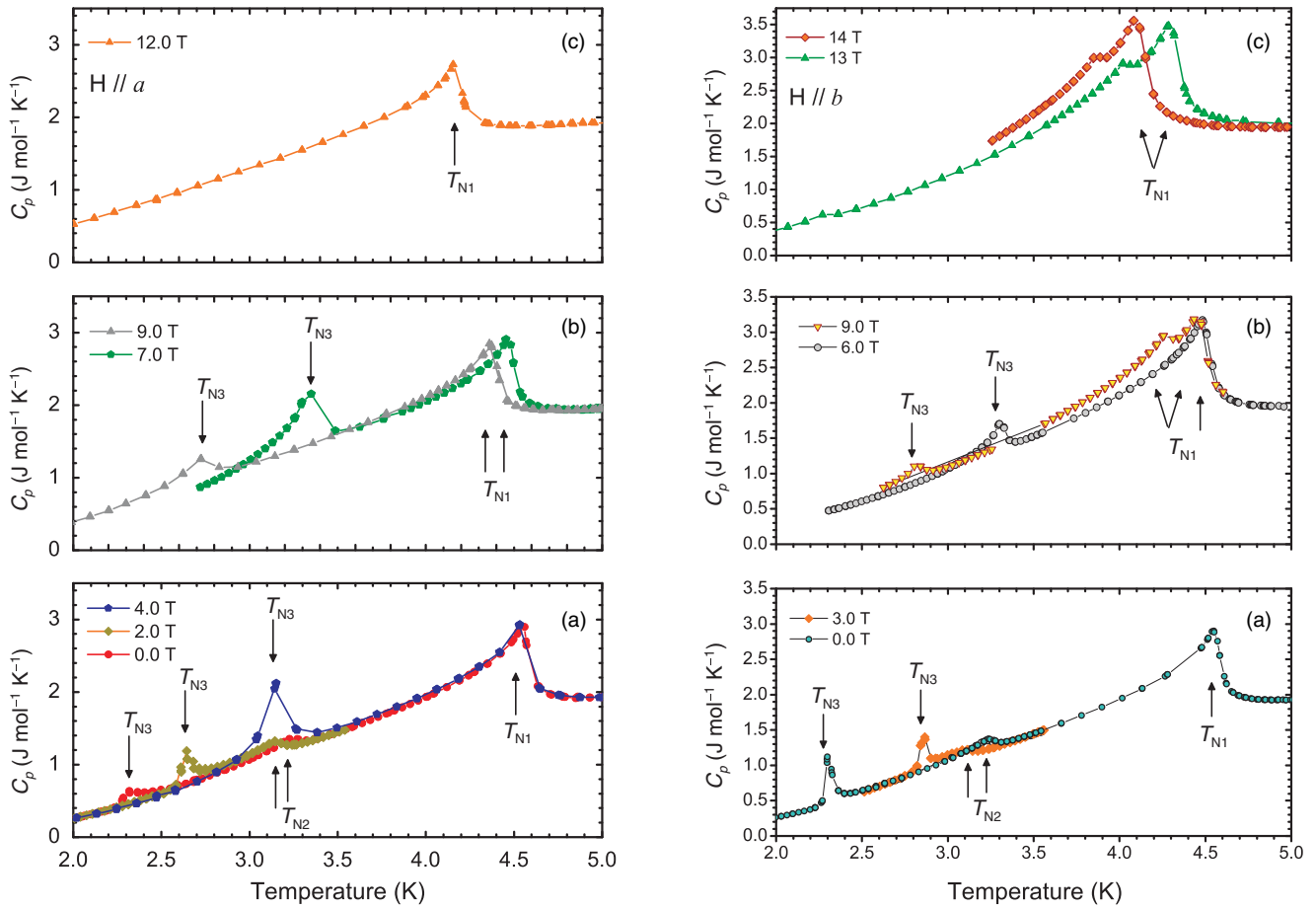
FIG. 4. (a)–(c) Specific heat vs temperature measured in the magnetic field applied along the b (left) and a (right) directions. Anomalies indicated with arrows are phase transitions.

that phase transitions displaying important lattice involvement become first order and develop hysteresis. In this case, hysteresis was not significant. We must point out, however, that our optical fiber technique is not the most appropriate for detection of thermal hysteresis as the fiber (the only contact

FIG. 5. Contraction of the c axis as a function of the increasing temperature in zero field, shown here to $T = 80$ K.

between the sample and sample holder) is a very poor thermal conductor and some thermal lag between the sample and thermometer is always present. Figures 6(b) and 6(c) display the magnetostriction obtained in a pulsed magnet to $H = 30$ T. The transition T_{N3} is visible as an increase in the lattice parameter with field, while T_{N1} appears split first as a decrease of the lattice parameter at 20 T then as a larger increase at 23 T.

Figure 6(a) (right) shows the thermal expansion measured along the chains in the direction c at constant magnetic fields in the low temperature region. T_{N1}, not visible in zero field, becomes clear as the magnetic field is increased to 14 T. T_{N2} and T_{N3}, on the other hand, look very similar to the $H\|b$ case. Figures 6(b) and 6(c) show the magnetostriction measured in pulsed magnetic fields, where the transitions T_{N3}, T_{N2}, and T_{N1} are clearly identified. While these transitions maintain similar characteristics for $H\|b$ and $H\|c$, the critical fields are significantly different. Figure 7 displays the magnetostriction in pulsed fields measured along the a axis, which shows anomalies at approximately 19 T and 22.5 T. At these anomalies the a axis behaves opposite to the b and c axes, pointing to a partial compensation of the expansion trend shown by those. The unit cell volume, hence, appears to expand as the sample magnetization is saturated by external magnetic fields.

Critical temperatures and critical fields identified in the above discussed magnetization $M(T,H)$, specific heat $C_p(T)$, thermal expansion $\mu\text{Strain}(T)$, and magnetostriction
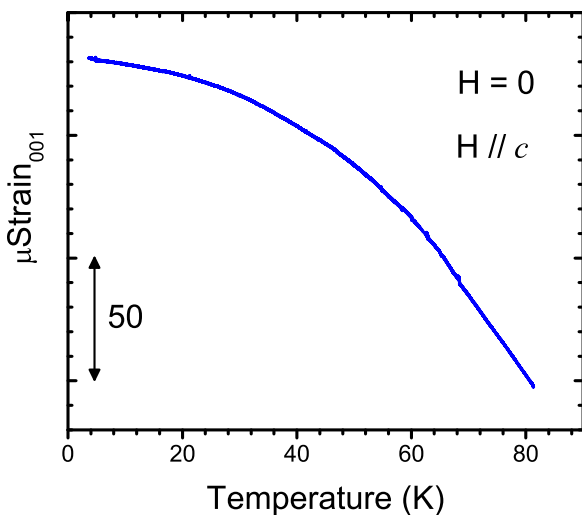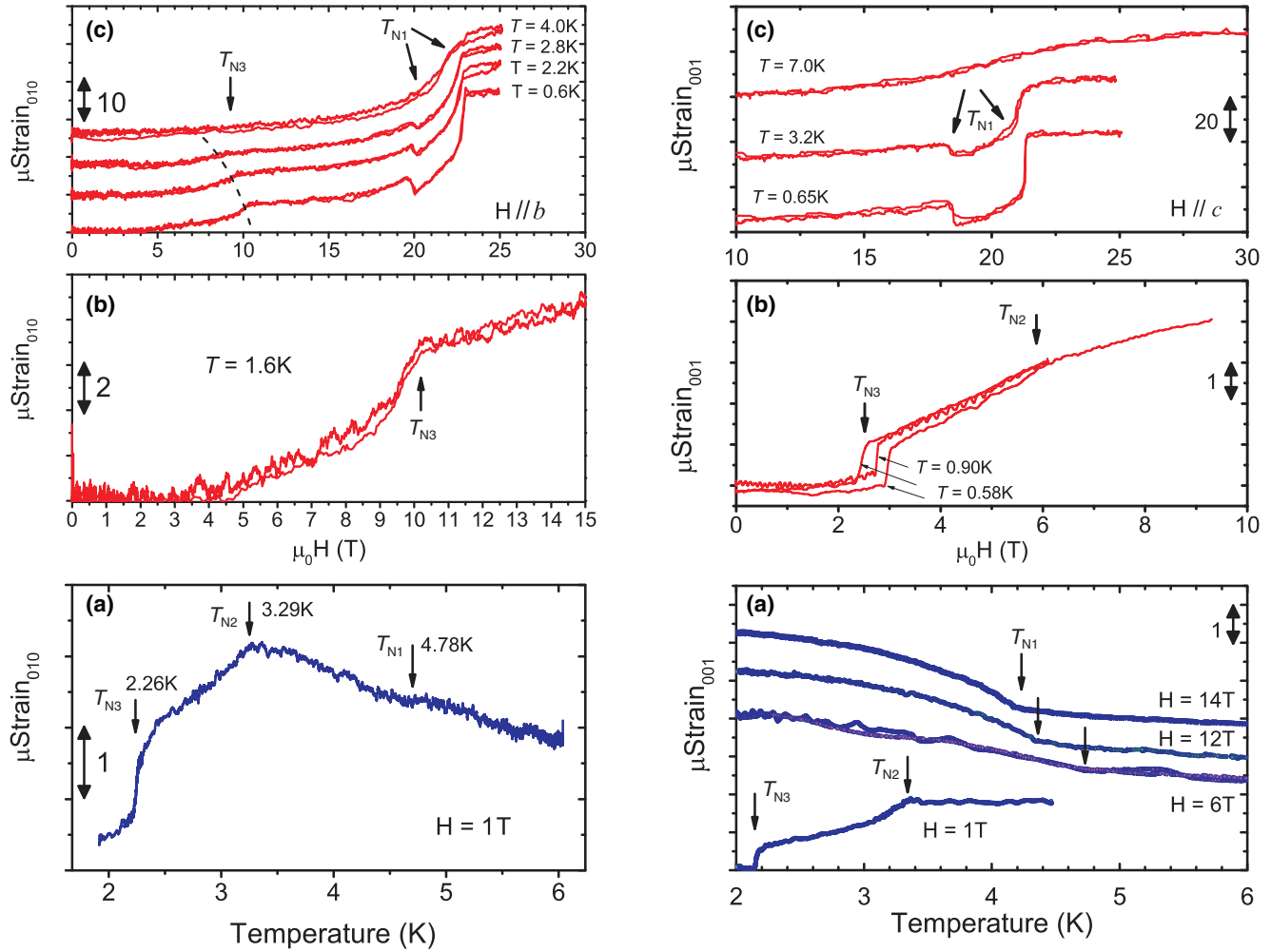
FIG. 6. Magnetostriction measured in fields applied along the b (left) and c (right) directions. The strain is measured along the field. (a) Evolution of the sample length vs temperature at constant magnetic field $H = 1$ T, showing anomalies at transition temperatures indicated by arrows; (b) and (c) magnetostriction in pulsed magnetic fields showing anomalies at fields indicated by arrows.

μStrain(H) were extracted and plotted in two phase diagrams displayed in Fig. 8. These plots reveal the previously unknown and intricate anisotropy, and the possibility of a tricritical point at $H = 20$ T, and $T \simeq 4$ K. By referring to zero-field neutron data [19], we identify the phase below T_{N3} as the helical order (H), the phase between T_{N2} and T_{N3} as the long-period stripe order (S), and the phase between T_{N1} and T_{N2} as the SDW order. The low-temperature helical phase is thus relatively stable in magnetic fields applied along a and b and becomes fragile when the field is applied along c, where, on the other hand, a broader region of the stripe phase is observed. Our observations are consistent with the results of Ref. [32], where temperature-field phase diagrams for two different field directions (a and c not resolved) were reported based on magnetic susceptibility measurements and below 5 T, only.

B. Crystal structure

The intricate temperature-field phase diagrams presented above cannot be understood without solid knowledge of the underlying crystal structure. According to Ref. [18], structural changes in β-TeVO$_4$ may happen around 150 K in the paramagnetic regime well above any magnetic transitions. To investigate this possibility, we performed high-resolution synchrotron XRD measurements at room temperature and at 10 K. No reflections violating the $P2_1/c$ symmetry could be seen in either of the patterns. Structure refinement revealed only weak temperature-induced structural changes. Most importantly, atomic displacement parameters decrease upon cooling, as expected in a well-ordered crystal structure. Therefore, we conclude that no drastic structural changes occur in β-TeVO$_4$ down to at least 10 K, and the orbital state of V^{4+} is robust. Our thermodynamic and magnetostriction measurements presented in Sec. III A further rule out any drastic structural changes at T_{N1} and T_{N2}, whereas the transition at T_{N3} should be coupled to the lattice. It is, however, well below the temperature range accessible for synchrotron XRD.

Upon cooling from room temperature to 10 K, the unit cell volume decreases by about 1%. Remarkably, this change is mostly related to the contraction of the a parameter, whereas the c parameter even increases by 0.05% in agreement with strain measurements in zero field (Fig. 5). This strongly anisotropic thermal expansion can be traced back to peculiarities of the crystal structure. The structural chains running along
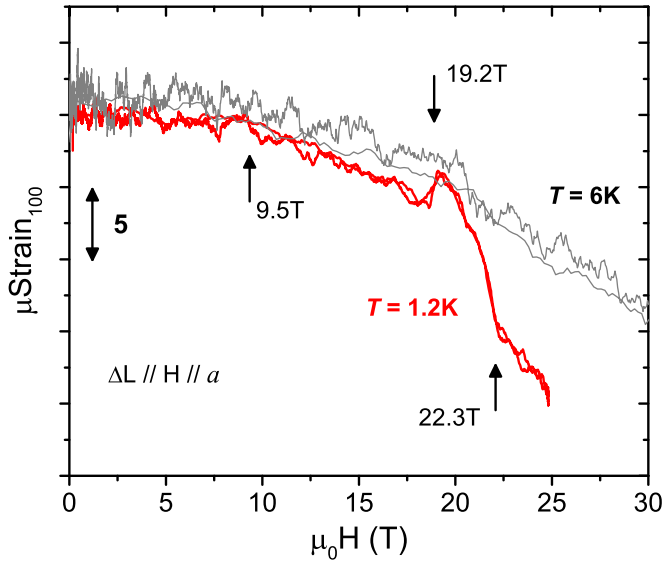
FIG. 7. Magnetostriction measured along the *a* direction in pulsed magnetic fields. Anomalies are indicated by arrows. As seen here, contrary to the *b* and *c* axis, the *a*-axis length contracts with applied fields. The lack of saturation at fields $H > 22$ T could be an artifact caused by magnetic torque on the sample.

the *c* direction are linked in the *bc* plane via TeO₄ pyramids (Fig. 1). The interlayer bonding is achieved via longer and thus weaker Te-O1 bonds of 2.95 Å, hence the *a* direction is most prone to expansion upon heating. The weak bonding along *a* is also consistent with the preferential cleaving of the β-TeVO₄ crystals perpendicular to the *a* direction.

C. ^{125}Te NMR

XRD probes long-range crystal structure in the bulk and may be less sensitive to structural changes that occur locally. Therefore, we also studied temperature evolution of β-TeVO₄ above its magnetic transitions using ^{125}Te NMR. The resonance frequency of the spin-1/2 ^{125}Te nucleus is determined by chemical shift interaction or, in magnetic materials, by the

magnetic hyperfine shift, the Knight shift, interaction. In solids as a rule, both interactions are anisotropic and described by a second-rank tensor. There are two pairs of tellurium Te^{4+} ions in the crystallographic unit cell (see Fig. 1, left). For an arbitrary direction of the magnetic field, the two neighboring Te ions of the same pair make equal projections, whereas the Te ions of the other pair have a different projection. Thus, one expects two ^{125}Te resonance lines in the spectrum of a single crystal at an arbitrary orientation of the magnetic field. Indeed, experiment shows two lines, which we denote as site 1 and site 2.

To determine the magnetic shift tensor, we performed three rotations of the single crystal around (approximately) the *a*, *b*, and *c* axes. The rotation patterns are given in Fig. 9. Following the standard procedure [33], one has to perform three subsequent transformations of the nuclear spin Hamiltonian: from the principal axis system (PAS) to the crystal frame, then to the goniometer frame, and eventually to the laboratory frame, and then the eigenvalues can be found. This way, we obtained the Knight shift tensor K with the principal components $K_{xx} = -0.67\%$, $K_{yy} = -0.40\%$, and $K_{zz} = +0.32\%$ (and the resulting isotropic value of $K_{iso} = -0.25\%$) equal for both Te^{4+} sites. The Euler angles $(\alpha; \beta; \gamma)$ for transforming the PAS of the K tensor to the crystal frame are $(106; 69; 110)$ degrees for site 1 and $(-106; -69; -110)$ degrees for site 2.

At lower temperatures, the NMR lines broaden, although no abrupt changes are observed around 150 K, where Gnezdilov *et al.* [18] expected a structural phase transition. The Knight shift (K) follows bulk magnetic susceptibility (χ), as shown in Fig. 10. From the slope of the Clogston-Jaccarino plot [34] K vs χ (inset of Fig. 10), we determine the hyperfine coupling constant as $H_{hf} = 2N_A\mu_B\Delta K/\Delta\chi$, where N_A is Avogadro's number, and μ_B is the Bohr magneton. For the two slightly differently oriented K tensors of Te, we obtain $H_{hf} = -55$ kOe/μ_B and $H_{hf} = -58$ kOe/μ_B.

Compared to the $H\|b$ case, the Knight shift in the $H\|a$ orientation is small, and its temperature dependence is rather weak (see Fig. 11, bottom). On the other hand, at low temperatures the line for $H\|a$ becomes nearly three times
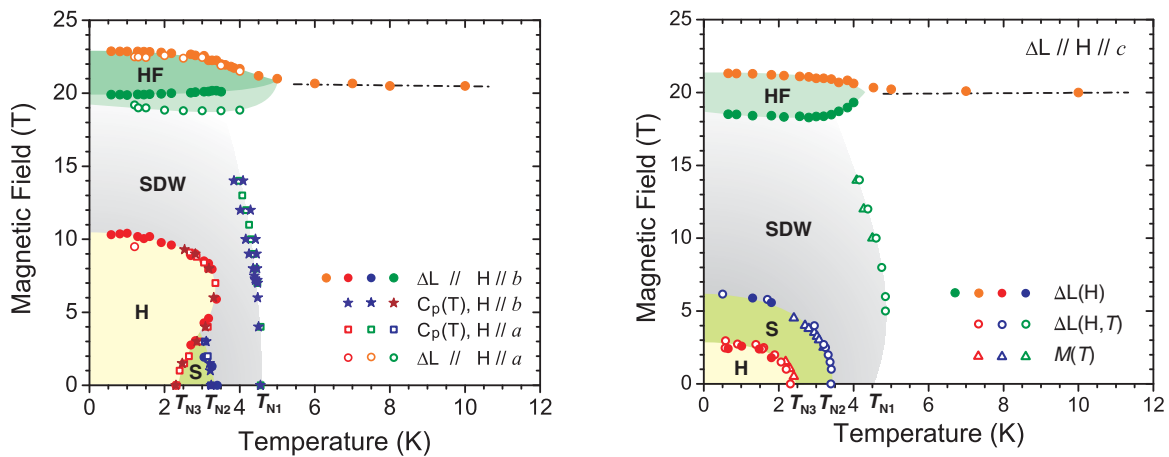

FIG. 8. Field-temperature phase diagram for β-TeVO₄ when the magnetic field is applied along the *a* and *b* axes (left) and along the *c* axis (right). The phases are labeled as follows: H (helical order), S (long-period stripe phase), SDW (spin-density wave), and HF (high-field phase of unknown origin, possibly a nematic phase).
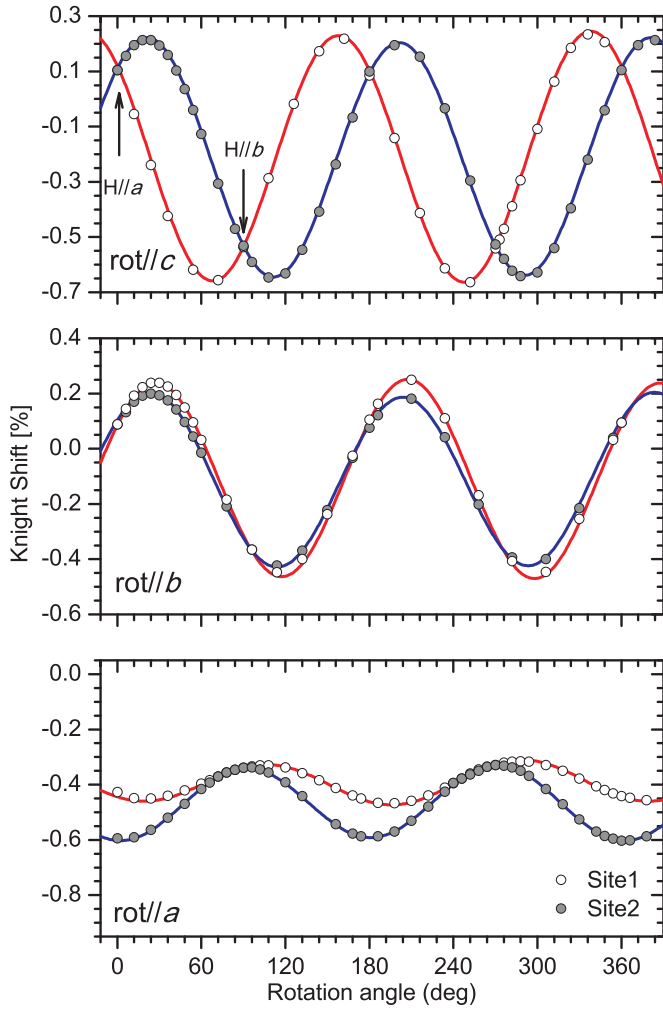
FIG. 9. ^{125}Te Knight shift versus goniometer rotation angle measured on the β-TeVO$_4$ single crystal at 285 K. The single crystal is rotated about the a, b, and c axes, as noted in the figure. The circles denote experimental frequencies; the full lines show the calculated angular dependence. The arrows denote orientations, where the temperature dependencies were measured.

broader than for the other orientations. The line broadening in the $H \| a$ direction is accompanied by an increase in the transverse relaxation rate $1/T_2$. Below 10 K, T_2 became shorter than a few μs, so that we could not record the line. For the two other directions, T_2 decreases by less than a factor of two, from 50 μs at 290 K to 30 μs at 10 K, from which down to T_{N1} it shortens again down to a few μs. Rapid shortening of the T_2 refers typically to the zero-frequency fluctuation of the local field along the external field. The spin-lattice relaxation time T_1 is found to be about 50 μs, almost independent of temperature and the crystal orientation.

D. Microscopic analysis

The complex magnetic behavior of β-TeVO$_4$ hinges upon its nontrivial crystal structure that gives rise to both isotropic and anisotropic magnetic couplings. Having established that the crystal structure remains unchanged down to T_{N1}, we will
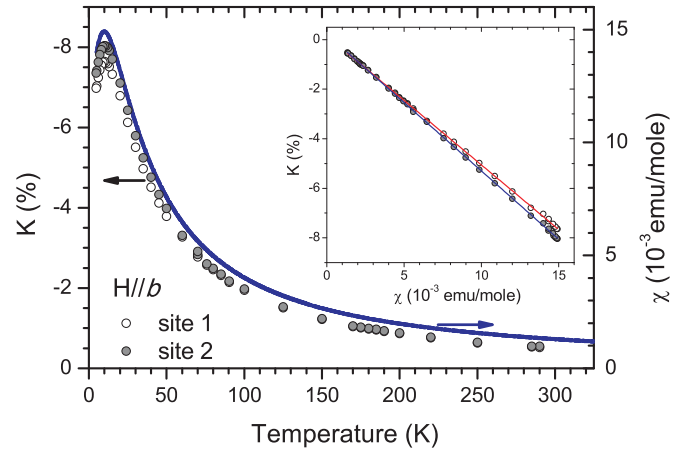

FIG. 10. Temperature dependence of the Knight shift K (full and empty circles, left scale) in the orientation $H \| b$ compared to the magnetic susceptibility curve for $H \| b$ (right scale, solid line) measured at 14 T. The two sites have slightly different orientations of the K tensor. The inset shows the perfectly linear K vs χ plot, where the slope gives the hyperfine coupling constant (see text).
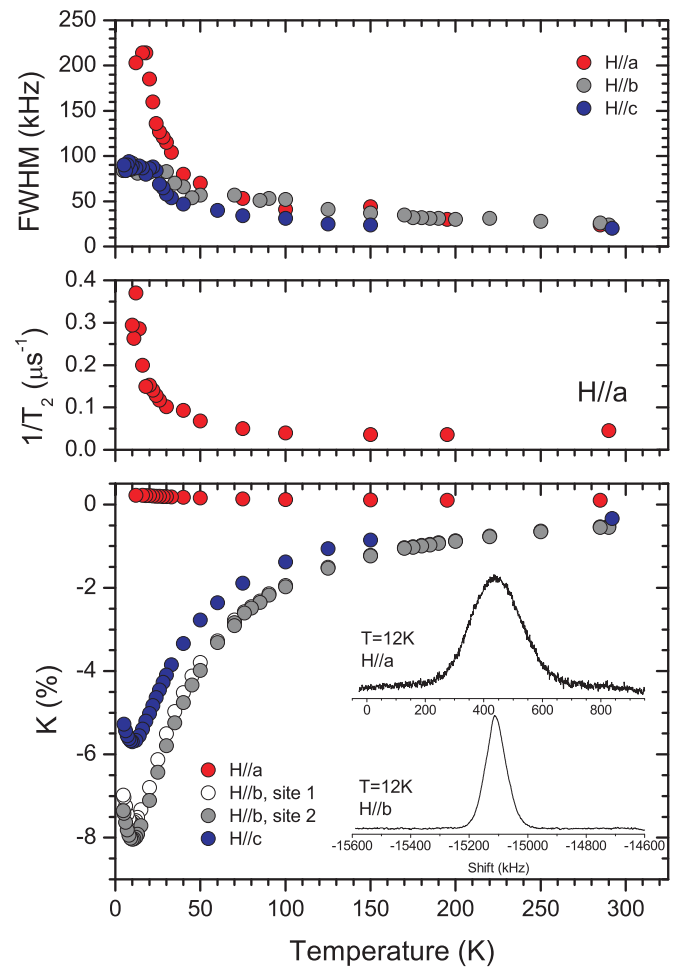

FIG. 11. Temperature dependence of the NMR linewidth (top panel), of the transverse relaxation rate in the $H \| a$ orientation (middle) and the Knight shift curves in three different orientations of the crystal. The inset shows the NMR lines recorded for the $H \| a$ and $H \| b$ orientations at 12 K.

TABLE I. Atomic positions in β-TeVO$_4$ refined from high-resolution synchrotron powder XRD. U_{iso} are isotropic atomic displacements parameters (ADPs) given in 10^{-2} Å^2. For each atom, the first line refers to the 10 K data, and the second line refers to the room-temperature data. The ADPs of oxygen atoms were constrained during the refinement. Lattice parameters are $a = 4.33989(2)$ Å, $b = 13.4943(1)$ Å, $c = 5.44460(3)$ Å, $\beta = 91.6572(2)°$ at 10 K, and $a = 4.38126(2)$ Å, $b = 13.5089(1)$ Å, $c = 5.44201(3)$ Å, $\beta = 91.6766(3)°$ at room temperature. The space group is $P2_1/c$.

	x/a	y/b	z/c	U_{iso}
Te	0.0421(1)	0.3911(1)	0.6431(1)	0.31(1)
	0.0392(1)	0.3911(1)	0.6430(1)	0.99(2)
V	0.6783(3)	0.1602(1)	0.6611(2)	0.36(3)
	0.6798(3)	0.1611(1)	0.6598(3)	0.65(4)
O1	0.3095(8)	0.1640(3)	0.6679(6)	0.18(5)
	0.296(1)	0.1643(4)	0.6674(8)	1.03(7)
O2	0.8310(8)	0.0480(3)	0.8633(7)	0.18(5)
	0.840(1)	0.0509(4)	0.8550(9)	1.03(7)
O3	0.8129(8)	0.2230(3)	0.9794(6)	0.18(5)
	0.816(1)	0.2244(4)	0.9824(9)	1.03(7)
O4	0.7501(8)	0.0828(2)	0.3713(6)	0.18(5)
	0.759(1)	0.0837(3)	0.3738(8)	1.03(7)

now use it to parametrize a microscopic spin Hamiltonian:

$$\hat{H} = \sum_{\langle ij \rangle} \left(J_{ij} \mathbf{S}_i \cdot \mathbf{S}_j + \mathbf{D}_{ij}[\mathbf{S}_i \times \mathbf{S}_j] + \mathbf{S}_i \cdot \Gamma_{ij} \cdot \mathbf{S}_j \right), \quad (1)$$

where the summation is over bonds of the spin lattice, J_{ij} are isotropic exchange couplings, $\mathbf{D}_{ij}$ are DM vectors (antisymmetric part of the exchange anisotropy), and Γ_{ij} tensors stand for the symmetric part of the anisotropy. We will evaluate the isotropic part of this Hamiltonian (J_{ij}) and rationalize several peculiarities of the low-temperature behavior. We will also analyze the anisotropic part qualitatively in order to underpin the difference between β-TeVO$_4$ and other J_1-J_2 frustrated-chain compounds.

1. Isotropic couplings

All calculations were performed for the experimental crystal structure of β-TeVO$_4$ determined at 10 K (Table I). Band structure calculated on the LDA level is shown in Fig. 12. Its apparent metallicity is related to the fact that LDA does not capture effects of strong electronic correlations pertinent to the 3d shell of V^{4+} [35]. We find predominantly V 3d states at the Fermi level. Crystal-field effects split the V 3d states into two narrow band complexes that can be ascribed [36] to the d_{xy} and $d_{yz} + d_{xz}$ orbitals around 0 and 1 eV, respectively. Above 1.2 eV, the spectrum is dominated by the $d_{x^2-y^2} + d_{3z^2-r^2}$ orbitals that strongly hybridize with Te 5p orbitals above 2.5 eV. The d_{xy} states have the lowest energy, in agreement with the crystal-field splitting expected for the fivefold oxygen coordination in the square pyramid.

The LDA band structure was analyzed using a 12-band tight-binding model, where we included all d_{xy}, d_{yz}, and d_{xz} bands lying between -0.3 eV and 1.0 eV. The hopping parameters t are then used to calculate individual exchange
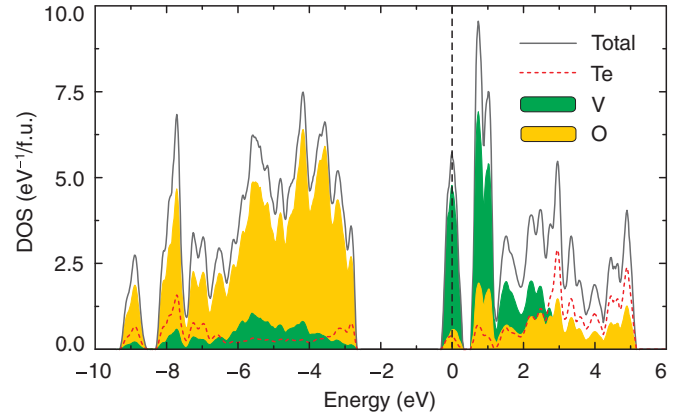

FIG. 12. LDA density of states for β-TeVO$_4$. The Fermi level is at zero energy. Note the crystal-field splitting of V 3d states and their hybridization with Te 5p above 2.5 eV.

integrals according to the Kugel-Khomskii model [37,38]:

$$J = \frac{4t_{xy \to xy}^2}{U_{\text{eff}}} - \sum_{\alpha = yz, xz} \frac{4 J_{\text{eff}} t_{xy \to \alpha}^2}{(U_{\text{eff}} + \Delta_\alpha)(U_{\text{eff}} - J_{\text{eff}} + \Delta_\alpha)}, \quad (2)$$

where ε_α are orbital energies, $\Delta_\alpha = \varepsilon_\alpha - \varepsilon_{xy}$ are crystal-field splittings, and $U_{\text{eff}} = 4$ eV and $J_{\text{eff}} = 1$ eV are the effective Coulomb repulsion and Hund's exchange in the V 3d shell, respectively [39,40]. The higher-lying d orbitals ($\alpha = 3z^2 - r^2, x^2 - y^2$) were excluded because of their strong mixing with the Te 5p states that render the fitting procedure somewhat ambiguous. We checked, however, that different fits, where the higher-lying orbitals were included, produce similar results and do not influence any of the conclusions drawn below.

In Table II, we list both FM and AFM contributions to the exchange corresponding to the second and first terms of Eq. (2), respectively. Alternatively, we evaluated exchange couplings by calculating total energies of several collinear spin configurations using DFT+U. Here, we used the generalized gradient approximation (GGA) [29], the on-site Coulomb repulsion $U_d = 4$ eV, the on-site Hund's exchange $J_d = 1$ eV, and the atomic-limit version of the double-counting correction term. We have also checked that a different double-counting correction scheme or different values of U_d lead to marginal

TABLE II. Interatomic distances $d_{\text{V-V}}$ (in Å) and isotropic exchange couplings J_i (in K) obtained from Eq. (2) and from total-energy GGA+U calculations. J_i^{AFM} and J_i^{FM} stand for the AFM and FM contributions to the exchange, according to the first and second terms of Eq. (2), respectively. For the notation of exchange couplings, see Fig. 1.

	$d_{\text{V-V}}$	J_i^{AFM}	J_i^{FM}	$J_i^{\text{Eq. (2)}}$	$J_i^{\text{GGA}+U}$
J_1	3.643	0.2	-41.8	-41.6	-26.2
J_2	5.445	71.4	-3.7	67.7	24.6
J_a	4.340	0.5	-1.1	-0.6	-0.5
J_{a1}	5.603	0.0	-1.8	-1.8	-2.2
J_{a2}	5.726	0.7	-1.2	-0.5	-0.5
J_{b1}	4.902	5.3	-4.3	1.0	1.0
J_{b2}	5.464	25.1	-2.3	22.8	7.3

changes in the exchange couplings without altering the resulting magnetic model.

Our results for the isotropic exchange couplings are in line with those from Ref. [16]. The two leading interactions are FM J_1 and AFM J_2 forming frustrated spin chains along the c direction. The strongest interchain coupling J_{b2} connects the chains in the bc plane, within the structural layers. The coupling between the layers is facilitated by FM J_a, J_{a1}, and J_{a2}. Other couplings along the a direction are below 0.2 K (by absolute value), and the couplings in the bc plane beyond J_{b2} are 2.0 K or less. Therefore, the magnetic model with J_1 and J_2 as intrachain couplings and J_{b2}, J_a, J_{a1}, and J_{a2} as interchain couplings provides an exhaustive microscopic description of β-TeVO$_4$ on the isotropic (Heisenberg) level.

The microscopic origin of these couplings can be understood as follows. The coupling J_1 involves only one oxygen atom and corresponds to the V-O-V pathway with the bridging angle of $133.6°$. While Goodenough-Kanamori-Anderson rules prescribe that such a coupling should be AFM, its AFM part is in fact negligible, and the FM part dominates. This is in line with the results of Ref. [16] and may be related to the enhanced hybridization between V $3d$ and Te $5p$ states. Te $5p$ orbitals contribute 6.5% of states in the vicinity of the Fermi level, which is comparable to 9.7% contributed by O $2p$ (see also Fig. 12). A somewhat similar microscopic scenario has been reported for CdVO$_3$ [38], where $5s$ orbitals of Cd admix to the V $3d$ states and trigger ferromagnetic exchange couplings that give rise to the overall ferromagnetic long-range order, a very rare case among V^{4+} oxides.

The couplings beyond J_1 are long range. Their mechanism is usually understood as V–O…O–V superexchange controlled by the V-O…O angles defining the linearity of the superexchange pathway, and by the O…O distance. Indeed, the larger values of J_2 and J_{b2} can be ascribed to the shortest O…O distances of 2.82–2.84 Å and 2.87 Å, respectively. In contrast, the longer O…O distance of 3.31 Å disfavors the interchain coupling J_{b1}, even though its V-V distance is 0.55 Å shorter than those of J_2 and J_{b2}. Finally, the weakly FM nature of J_a, J_{a1}, and J_{a2} is typical for interactions in the direction perpendicular to basal planes of VO$_5$ pyramids, as in Pb$_2$V$_3$O$_9$ [39] and Zn$_2$VO(PO$_4$)$_2$ [41]. Here, no suitable V–O…O–V pathway for an efficient $xy \rightarrow xy$ hopping can be formed, hence the AFM contribution is very small. On the other hand, the V–V distance is short enough to induce nonzero $xy \rightarrow yz$ and $xy \rightarrow xz$ hoppings resulting in weakly FM superexchange.

2. Comparison to the experiment

In β-TeVO$_4$, frustrated interactions J_1 and J_2 along spin chains manifest themselves already in thermodynamic properties. In Fig. 13, we compare both temperature dependence of the magnetic susceptibility and field dependence of the magnetization with two models: (i) the uniform Heisenberg chain (HC) proposed in Ref. [15] and (ii) the J_1-J_2 frustrated Heisenberg chain (FHC) supported by our calculations. Both models provide good fits of the magnetic susceptibility resulting in $J = 20.2$ K, $g = 2.09$ for the HC, and $J_2 = -J_1 = 26.4$ K, $g = 2.00$ for the FHC. However, a closer examination of the difference between the simulated
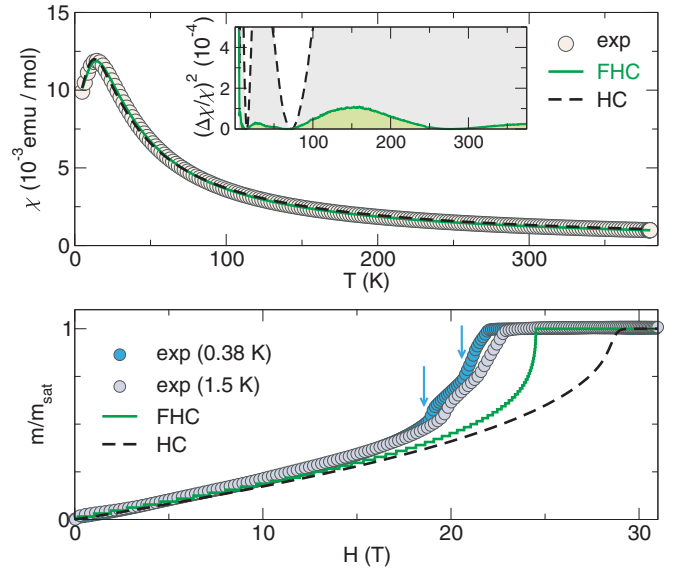

FIG. 13. Top: experimental magnetic susceptibility fitted with the uniform Heisenberg chain (HC) and frustrated Heisenberg chain (FHC) models. The inset shows the difference between the experimental and simulated curves, as defined in the text. Bottom: experimental magnetization curve compared to the model predictions with no adjustable parameters.

and experimental curves ($\Delta\chi = (\chi_{calc} - \chi_{exp})^2/\chi_{exp}^2$) reveals better agreement for the FHC model (Fig. 13, top inset). This model also provides a better description of the high-field magnetization curve, although the saturation field is slightly overestimated. Finally, the fitted g value for the FHC model is in good agreement with $g = 2.01$ measured by electron spin resonance [19], while the fitted g value for the HC model would be too high.

We can now rationalize the incommensurate magnetic order that has been observed in β-TeVO$_4$ experimentally [19]. The propagation vector $\mathbf{k} = (-0.208, 0, 0.423)$ below T_{N3} implies the pitch angle $\alpha = 76.1°$ for the helix propagating along the c direction. This is in very good agreement with $J_2/J_1 = -1$ that yields the classical pitch angle $\alpha_{cl} = \arccos(-J_1/4J_2) = 75.5°$, whereas quantum corrections to the pitch angle are small in this range of J_2/J_1 [1].

The leading interchain coupling along the b direction, J_{b2}, is compatible with the helical order and leads to the same spin arrangement within every second chain, so that, e.g., both atoms 3 in Fig. 1 (middle) feature parallel spins resulting in $k_y = 0$. On the other hand, the FM interchain couplings are incompatible with the helical order (Fig. 14, left). The couplings J_1, J_a, and J_{a1} (J_{a2}) build triangles, where the noncollinear order of the two spins coupled by J_1 cannot be combined with the FM order imposed by J_a and J_{a1} (J_{a2}). This frustration is alleviated by introducing a noncollinear spin arrangement on J_a and J_{a1} (J_{a2}) too. By a classical energy minimization for the magnetic model defined by the exchange couplings from Table II [42], we find that the spins on atoms 1 and 1* should be turned by an angle

$$\varphi = \arctan\left[\frac{(J_{a2} - J_{a1})\sin\alpha}{(J_{a2} + J_{a1})\cos\alpha + J_a}\right] \simeq -53.9° \quad (3)$$
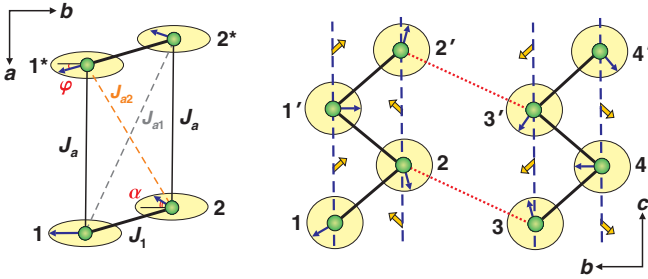
FIG. 14. Formation of the helical magnetic structure in β-TeVO$_4$. Left panel: the competition between the helical structure along the chain and the FM interchain couplings (J_a, J_{a1}, J_{a2}), resulting in a phase shift φ between the neighboring helices along the a directions. Right panel: same direction of rotation (counter clockwise in this case) in the chains 1-2 and 3-4 is imposed by the AFM interchain coupling J_{b2}. It is, however, incompatible with the DM vectors $\mathbf{D}_2$ (shown by orange arrows) that change sign from $(d_{2x}, \pm d_{2y}, d_{2z})$ to $(-d_{2x}, \mp d_{2y}, -d_{2z})$ upon going from the chain 1-2 to the chain 3-4. Note that the bc plane is arbitrarily chosen as the helix plane for the sake of better visualization.

corresponding to $k_x = \varphi/360 = -0.150$, which is somewhat lower than $k_x = -0.208$ in the experiment but shows the correct sign and explains the opposite directions of rotation along a and c.

We find that the incommensurability along the a direction is controlled by a rather subtle difference between the diagonal interactions J_{a1} and J_{a2} that correspond to the bond vectors $(1, \Delta y, \frac{1}{2})$ and $(1, \Delta y, -\frac{1}{2})$, respectively, where $\Delta y = 0.1796$ is the difference between the y coordinates of the two neighboring V atoms along the chain. The interaction J_{a1} is more FM than J_{a2}. Therefore, the angle φ has to counteract the rotation introduced by α in order to bring spins 1 and 2* connected by J_{a1} closer to the parallel configuration.

3. Magnetic anisotropy

In the following, we extend our microscopic analysis to the anisotropy parameters entering Eq. (1). Technically, these parameters could be evaluated in the same spirit of perturbation theory as in Eq. (2), following Refs. [43,44]. However, the evaluation of magnetic anisotropy requires that hoppings to all four unoccupied d orbitals, including $d_{x^2-y^2}$ and $d_{3z^2-r^2}$, are defined, which is not the case in β-TeVO$_4$, where the strong hybridization between Te $5p$ and V $3d$ orbitals prevents unambiguous modeling of the higher-lying d bands. Therefore, we restrict ourselves to a qualitative analysis that provides useful insight into the role of magnetic anisotropy in β-TeVO$_4$.

The DM terms are allowed by symmetry for both intrachain couplings. Symmetry relations between different components of the $\mathbf{D}_1$ and $\mathbf{D}_2$ on individual lattice bonds are summarized in Table III. Helical ground state implies that the same rotations occur between every two contiguous spins in a chain (Fig. 14). Since all three components of $\mathbf{D}_1$ change sign within the chain, the nearest-neighbor DM couplings do not gain any energy from the helical order. The same argument shows that d_{2y} cannot stabilize the helical order, because it changes sign between $\mathbf{D}_2^{(11')}$ and $\mathbf{D}_2^{(22')}$. On the other hand, d_{2x} and d_{2z} gain energy from the helical order and should thus stabilize the helix

TABLE III. DM couplings in β-TeVO$_4$. For the notation of the V^{4+} sites 1–4, see Figs. 1 and 14.

$\mathbf{D}_1^{(12)} =$	(d_{1x}, d_{1y}, d_{1z})	$\mathbf{D}_2^{(11')} =$	(d_{2x}, d_{2y}, d_{2z})
$\mathbf{D}_1^{(21')} =$	$(-d_{1x}, -d_{1y}, -d_{1z})$	$\mathbf{D}_2^{(22')} =$	$(d_{2x}, -d_{2y}, d_{2z})$
$\mathbf{D}_1^{(34)} =$	(d_{1x}, d_{1y}, d_{1z})	$\mathbf{D}_2^{(33')} =$	$(-d_{2x}, -d_{2y}, -d_{2z})$
$\mathbf{D}_1^{(34')} =$	$(-d_{1x}, -d_{1y}, -d_{1z})$	$\mathbf{D}_2^{(44')} =$	$(-d_{2x}, d_{2y}, -d_{2z})$

in the plane perpendicular to $(d_{2x}, 0, d_{2z})$ within the 1-2 chain. However, the relevant DM components in the neighboring 3-4 chains are $(-d_{2x}, 0, -d_{2z})$ implying that the helix with the opposite sense of rotation will be stabilized. On the other hand, the AFM interchain coupling J_{b2} imposes the same sense of rotation in the helices 1-2 and 3-4 (Fig. 14, right).

The sign change of $\mathbf{D}_2$ between the two contiguous chains implies that the helix plane in β-TeVO$_4$ cannot be uniquely defined when the DM anisotropy is considered. This striking observation should be paralleled to the following. First, the helical order is stabilized only below T_3 upon a first-order phase transition that entails an abrupt shrinkage of the unit cell along the b and c directions implying a structural effect that probably alleviates this frustration. Second, neutron-scattering data indicate two different helix planes for the chains 1-2 and 3-4, respectively [45]. This observation is hard to reconcile with the monoclinic crystal structure of β-TeVO$_4$, where these two chains are crystallographically equivalent (related by an inversion symmetry), and thus a structural distortion must be involved.

The incompatibility of the helical order with the DM anisotropy in β-TeVO$_4$ is also a plausible reason behind the delayed formation of the helical phase upon cooling in zero field. Other J_1-J_2 frustrated-chain compounds reported so far [22] undergo a direct (and second-order) transition from the paramagnetic phase to the helically-ordered phase in zero field. In β-TeVO$_4$, however, the paramagnetic and helically-ordered phases are separated by the SDW phase (between T_{N1} and T_{N2}) and by the long-period stripe order (between T_{N2} and T_{N3}), see Fig. 8. We can also conclude that the helical order is largely destabilized in the magnetic field applied along the c direction (compare the two panels of Fig. 8), which should then be the common direction of the two helices, i.e., the direction that is most vulnerable to the application of the magnetic field.

IV. DISCUSSION AND SUMMARY

β-TeVO$_4$ is a structurally perfect material prototype of the J_1-J_2 frustrated spin-chain model. Our data rule out any structural distortions preceding magnetic transitions in this compound and clearly exclude any change in the orbital state of V^{4+} upon cooling. On the other hand, magnetic anisotropy triggered by the low crystallographic symmetry introduces a very complex behavior, especially in low magnetic fields. By comparing temperature-field phase diagrams obtained for different field directions, we conclude that the transitions at T_{N2} and T_{N3} are strongly direction dependent and should be influenced or even triggered by the presence of magnetic anisotropy. The field evolution of T_{N1} is, at first glance, reminiscent of a conventional long-range AFM ordering and

reveals no appreciable anisotropy. Finally, the high-field phase emerging above 18 T turns out to be weakly dependent on the field direction and thus nearly isotropic.

The emergence of the high-field phase for different field directions indicates its relation to the physics of the isotropic J_1-J_2 spin chain. This phase can be ascribed to the multipolar order or nematic state envisaged in recent theoretical studies [13,46,47]. The multipolar order should be robust with respect to the interchain couplings at $J_2/J_1 \simeq -1$ [14], which renders β-TeVO$_4$ a good model material for studying high-field physics of the frustrated J_1-J_2 spin chain. Further investigation of this high-field phase is highly desirable.

In lower fields, we observed that the helical phase is destabilized by the magnetic field $H\|c$ and gives way to a larger region of the long-period stripe order, while for other field directions the stripe phase shrinks to a small pocket visible in low magnetic fields only. Both helical and spin-density-wave phases are incommensurate along both a and c [19]. While the incommensurability along the c direction is a natural result of the intrachain frustration, the incommensurability along a can be understood as a competition of ferromagnetic interchain couplings with the helical (or spin-density-wave) order within the chain.

Regarding magnetic anisotropy, β-TeVO$_4$ is different from any other J_1-J_2 frustrated-spin-chain compound reported so far. Materials like CuGeO$_3$ and NaCu$_2$O$_2$ lack DM couplings completely, because inversion centers are found in the middle of both nearest-neighbor and next-nearest-neighbor bonds. In LiCuVO$_4$ and linarite, inversion symmetry forbids $\mathbf{D}_2$, whereas $\mathbf{D}_1$ may be nonzero, although its exact magnitude is still unknown. Finally, β-TeVO$_4$ has inversion centers between the chains only. Therefore, all DM couplings are nonzero, and the symmetry of $\mathbf{D}_2$ is compatible with the helical order, thus providing additional stabilization energy for each helix but impeding the order between the helices. This frustration of anisotropic exchange couplings may be the crux of the β-TeVO$_4$ physics in low magnetic fields that awaits further investigation with direct methods, such as neutron scattering in applied magnetic field.

[1] R. Zinke, S.-L. Drechsler, and J. Richter, Influence of interchain coupling on spiral ground-state correlations in frustrated spin-(1/2) $J_1 - J_2$ Heisenberg chains, Phys. Rev. B **79**, 094425 (2009).

[2] S. Furukawa, M. Sato, and S. Onoda, Chiral Order and Electromagnetic Dynamics in One-Dimensional Multiferroic Cuprates, Phys. Rev. Lett. **105**, 257205 (2010).

[3] S. Park, Y. J. Choi, C. L. Zhang, and S.-W. Cheong, Ferroelectricity in an $S = 1/2$ Chain Cuprate, Phys. Rev. Lett. **98**, 057601 (2007).

[4] F. Schrettle, S. Krohns, P. Lunkenheimer, J. Hemberger, N. Büttgen, H.-A. Krug von Nidda, A. V. Prokofiev, and A. Loidl, Switching the ferroelectric polarization in the $S = 1/2$ chain cuprate LiCuVO$_4$ by external magnetic fields, Phys. Rev. B **77**, 144101 (2008).

[5] Li Zhao, Tsu-Lien Hung, Ching-Chien Li, Yang-Yuan Chen, Maw-Kuen Wu, R. K. Kremer, M. G. Banks, A. Simon, M.-H. Whangbo, C. Lee, J. S. Kim, I. Kim, and K. H. Kim, CuBr$_2$–a new multiferroic material with high critical temperature, Adv. Mater. **24**, 2469 (2012).

[6] For a brief review, see: O. A. Starykh, Unusual ordered phases of highly frustrated magnets: a review, Rep. Prog. Phys. **78**, 052502 (2015).

[7] N. Büttgen, W. Kraetschmer, L. E. Svistov, L. A. Prozorova, and A. Prokofiev, NMR study of the high-field magnetic phase of LiCuVO$_4$, Phys. Rev. B **81**, 052403 (2010).

[8] T. Masuda, M. Hagihala, Y. Kondoh, K. Kaneko, and N. Metoki, Spin density wave in insulating ferromagnetic frustrated chain LiCuVO$_4$, J. Phys. Soc. Jpn. **80**, 113705 (2011).

[9] M. Mourigal, M. Enderle, B. Fåk, R. K. Kremer, J. M. Law, A. Schneidewind, A. Hiess, and A. Prokofiev, Evidence of a Bond-Nematic Phase in LiCuVO$_4$, Phys. Rev. Lett. **109**, 027203 (2012).

[10] L. E. Svistov, T. Fujita, H. Yamaguchi, S. Kimura, K. Omura, A. Prokofiev, A. I. Smirnov, Z. Honda, and M. Hagiwara, New high magnetic field phase of the frustrated $s = \frac{1}{2}$ chain compound LiCuVO$_4$, JETP Lett. **93**, 21 (2011).

[11] N. Büttgen, K. Nawa, T. Fujita, M. Hagiwara, P. Kuhns, A. Prokofiev, A. P. Reyes, L. E. Svistov, K. Yoshimura, and M. Takigawa, Search for a spin-nematic phase in the quasi-one-dimensional frustrated magnet LiCuVO$_4$, Phys. Rev. B **90**, 134401 (2014).

[12] T. Hikihara, L. Kecke, T. Momoi, and A. Furusaki, Vector chiral and multipolar orders in the spin-(1/2) frustrated ferromagnetic chain in magnetic field, Phys. Rev. B **78**, 144404 (2008).

[13] J. Sudan, A. Lüscher, and A. M. Läuchli, Emergent multipolar spin correlations in a fluctuating spiral: The frustrated ferromagnetic spin-$\frac{1}{2}$ Heisenberg chain in a magnetic field, Phys. Rev. B **80**, 140402(R) (2009).

[14] S. Nishimoto, S.-L. Drechsler, R. Kuzian, J. Richter, and J. van den Brink, Interplay of interchain interactions and exchange anisotropy: Stability and fragility of multipolar states in spin-$\frac{1}{2}$ quasi-one-dimensional frustrated helimagnets, Phys. Rev. B **92**, 214415 (2015).

[15] Yu. Savina, O. Bludov, V. Pashchenko, S. L. Gnatchenko, P. Lemmens, and H. Berger, Magnetic properties of the antiferromagnetic spin-1/2 chain system β-TeVO$_4$, Phys. Rev. B **84**, 104447 (2011).

[16] A. Saúl and G. Radtke, Density functional approach for the magnetism of β-TeVO$_4$, Phys. Rev. B **89**, 104414 (2014).

[17] Yu. O. Savina, A. N. Bludov, V. A. Pashchenko, S. L. Gnatchenko, Yu. V. Savin, S. Schäfer, P. Lemmens, and H. Berger, A study of the magnetic properties of a quasi-one-dimensional magnet β-TeVO$_4$ in the frame of the $J_1 - J_2$ model, Low Temp. Phys. **41**, 659 (2015).

[18] V. Gnezdilov, P. Lemmens, D. Wulferding, Yu. Pashkevich, K. Lamonova, K.-Y. Choi, O. Afanasiev, S. Gnatchenko, and H. Berger, Low-dimensional magnetism of spin-$\frac{1}{2}$ chain systems of α- and β-TeVO$_4$: A comparative study, Low Temp. Phys. **38**, 559 (2012).

[19] M. Pregelj, A. Zorko, O. Zaharko, H. Nojiri, H. Berger, L. C. Chapon, and D. Arcon, Spin-stripe phase in a frustrated zigzag spin-$\frac{1}{2}$ chain, Nature Comm. **6**, 7255 (2015).

[20] G. Meunier, J. Darriet, and J. Galy, L'oxyde double TeVO$_4$ II. Structure cristalline de TeVO$_4$-β-relations structurales, J. Solid State Chem. **6**, 67 (1973).

[21] A. U. B. Wolter, F. Lipps, M. Schäpers, S.-L. Drechsler, S. Nishimoto, R. Vogel, V. Kataev, B. Büchner, H. Rosner, M. Schmitt, M. Uhlarz, Y. Skourski, J. Wosnitza, S. Süllow, and K. C. Rule, Magnetic properties and exchange integrals of the frustrated chain cuprate linarite PbCuSO$_4$(OH)$_2$, Phys. Rev. B **85**, 014407 (2012).

[22] M. Schäpers, A. U. B. Wolter, S.-L. Drechsler, S. Nishimoto, K.-H. Müller, M. Abdel-Hafiez, W. Schottenhamel, B. Büchner, J. Richter, B. Ouladdiaf, M. Uhlarz, R. Beyer, Y. Skourski, J. Wosnitza, K. C. Rule, H. Ryll, B. Klemke, K. Kiefer, M. Reehuis, B. Willenberg, and S. Süllow, Thermodynamic properties of the anisotropic frustrated spin-chain compound linarite PbCuSO$_4$(OH)$_2$, Phys. Rev. B **88**, 184410 (2013).

[23] M. Jaime, R. Daou, S. A. Crooker, F. Weickert, A. Uchida, A. E. Feiguin, C. D. Batista, H. A. Dabkowska, and B. D. Gaulin, Magnetostriction and magnetic texture to 100.75 Tesla in frustrated SrCu$_2$(BO$_3$)$_2$, Proc. Nat. Acad. Sci. USA **109**, 12404 (2012).

[24] R. Daou, F. Weickert, M. Nicklas, F. Steglich, A. Haase, and M. Doerr, High resolution magnetostriction measurements in pulsed magnetic fields using fiber Bragg gratings, Rev. Sci. Instrum. **81**, 033909 (2010).

[25] V. Petříček, M. Dušek, and L. Palatinus, *Jana2006. The crystallographic computing system* (Institute of Physics, Praha, Czech Republic, 2006).

[26] K. Momma and F. Izumi, *VESTA*3 for three-dimensional visualization of crystal, volumetric and morphology data, J. Appl. Crystallogr. **44**, 1272 (2011).

[27] K. Koepernik and H. Eschrig, Full-potential nonorthogonal local-orbital minimum-basis band-structure scheme, Phys. Rev. B **59**, 1743 (1999).

[28] J. P. Perdew and Y. Wang, Accurate and simple analytic representation of the electron-gas correlation energy, Phys. Rev. B **45**, 13244 (1992).

[29] J. P. Perdew, K. Burke, and M. Ernzerhof, Generalized Gradient Approximation Made simple, Phys. Rev. Lett. **77**, 3865 (1996).

[30] X. Wang and T. Xiang, Transfer-matrix density-matrix renormalization-group theory for thermodynamics of one-dimensional quantum system, Phys. Rev. B **56**, 5061 (1997).

[31] A.F. Albuquerque, F. Alet, P. Corboz, P. Dayal, A. Feiguin, S. Fuchs, L. Gamper, E. Gull, S. Gürtler, A. Honecker, R. Igarashi,

M. Körner, A. Kozhevnikov, A. Läuchli, S.R. Manmana, M. Matsumoto, I.P. McCulloch, F. Michel, R.M. Noack, G. Pawłowski, L. Pollet, T. Pruschke, U. Schollwöck, S. Todo, S. Trebst, M. Troyer, P. Werner, and S. Wessel, The ALPS project release 1.3: Open-source software for strongly correlated systems, J. Magn. Magn. Mater. **310**, 1187 (2007).

[32] Yu. O. Savina, O. M. Bludov, V. A. Pashchenko, S. L. Gnatchenko, P. Lemmens, and H. Berger, Features of the magnetic properties of quasi-one-dimensional β-TeVO$_4$ magnets at low temperatures, Low Temp. Phys. **41**, 283 (2015).

[33] M. Mehring, *NMR spectroscopy in solids* (Springer-Verlag, Berlin, Heidelberg, New-York, 1976).

[34] A. M. Clogston and V. Jaccarino, Susceptibilities and negative Knight shifts of intermetallic compounds, Phys. Rev. **121**, 1357 (1961).

[35] Note that in DFT+U we reproduce the insulating state with a band gap of about 3.0 eV.

[36] Here, we used the coordinate frame with the z axis directed along the short V-O bond in the axial position of the VO$_5$ square pyramids. The x and y axes are directed roughly toward the oxygen atoms in the basal plane of the pyramid, subject to a condition that x and y should be perpendicular to z.

[37] V. V. Mazurenko, F. Mila, and V. I. Anisimov, Electronic structure and exchange interactions of Na$_2$V$_3$O$_7$, Phys. Rev. B **73**, 014418 (2006).

[38] A. A. Tsirlin, O. Janson, and H. Rosner, Unusual ferromagnetic superexchange in CdVO$_3$: The role of Cd, Phys. Rev. B **84**, 144429 (2011).

[39] A. A. Tsirlin and H. Rosner, *Ab initio* modeling of Bose-Einstein condensation in Pb$_2$V$_3$O$_9$, Phys. Rev. B **83**, 064415 (2011).

[40] A. A. Tsirlin, R. Nath, J. Sichelschmidt, Y. Skourski, C. Geibel, and H. Rosner, Frustrated couplings between alternating spin-$\frac{1}{2}$ chains in AgVOAsO$_4$, Phys. Rev. B **83**, 144412 (2011).

[41] S. M. Yusuf, A. K. Bera, N. S. Kini, I. Mirebeau, and S. Petit, Two- and three-dimensional magnetic correlations in the spin-1/2 square-lattice system Zn$_2$VO(PO$_4$)$_2$, Phys. Rev. B **82**, 094412 (2010).

[42] Here, we fixed the angle between spins 1 and 2 to the pitch angle of the helix α. We checked that the simultaneous variation of φ and α leads to a nearly indistinguishable result, because the value of α is fixed by a much larger energy scale of $J_2 \simeq -J_1 \simeq 25$ K.

[43] V. V. Mazurenko, S. L. Skornyakov, V. I. Anisimov, and F. Mila, First-principles investigation of symmetric and antisymmetric exchange interactions of SrCu$_2$(BO$_3$)$_2$, Phys. Rev. B **78**, 195110 (2008).

[44] A. Vasiliev, O. Volkova, E. Zvereva, M. Isobe, Y. Ueda, S. Yoshii, H. Nojiri, V. Mazurenko, M. Valentyuk, V. Anisimov, I. Solovyev, R. Klingeler, and B. Büchner, Barium vanadium silicate BaVSi$_2$O$_7$: A t_{2g} counterpart of the Han purple compound, Phys. Rev. B **87**, 134412 (2013).

[45] O. Zaharko, M. Pregelj, A. Zorko, H. Nojiri D. Arcon, T. Morioka, and H. Berger, Spin-$\frac{1}{2}$ frustrated zigzag chain compound β-TeVO$_4$, Acta Crystallogr. Sect. A **A70**, C1545 (2014).

[46] M. E. Zhitomirsky and H. Tsunetsugu, Magnon pairing in quantum spin nematic, Europhys. Lett. **92**, 37001 (2010).

[47] M. Sato, T. Hikihara, and T. Momoi, Spin-Nematic and Spin-Density-Wave Orders in Spatially Anisotropic Frustrated Magnets in a Magnetic Field, Phys. Rev. Lett. **110**, 077206 (2013).